View metadata, citation and similar papers at core.ac.uk
brought to you by CORE
provided by NASA Technical Reports Server

Dynamic Smagorinsky Modeled Large-Eddy Simulations of Turbulence Using Tetrahedral Meshes

Chau-Lyan Chang[1]
NASA Langley Research Center, Hampton, VA 23681

and

Balaji Venkatachari[2]
National Institute of Aerospace, Hampton, VA 23666

Eddy-resolving numerical computations of turbulent flows are emerging as viable alternatives to Reynolds Averaged Navier-Stokes (RANS) calculations for flows with an intrinsically steady mean state due to the advances in large-scale parallel computing. In these computations, medium to large turbulent eddies are resolved by the numerics while the smaller or subgrid scales are either modeled or taken care of by the inherent numerical dissipation. To advance the state of the art of unstructured-mesh turbulence simulation capabilities, large eddy simulations (LES) using the dynamic Smagorinsky model (DSM) on tetrahedral meshes are carried out with the space-time conservation element, solution element (CESE) method. In contrast to what has been reported in the literature, the present implementation of dynamic models allows for active backscattering without any ad-hoc limiting of the eddy viscosity calculated from the subgrid-scale model. For the benchmark problems involving compressible isotropic turbulence decay as well as the shock/turbulent boundary layer interaction benchmark problems, no numerical instability associated with kinetic energy growth is observed and the volume percentage of the backscattering portion accounts for about 38-40% of the simulation domain. A slip-wall model in conjunction with the implemented DSM is used to simulate a relatively high Reynolds number Mach 2.85 turbulent boundary layer over a $30°$ ramp with several tetrahedral meshes and a wall-normal spacing of either $\Delta y^+ = 10$ or $\Delta y^+ = 20$. The computed mean wall pressure distribution, separation region size, mean velocity profiles, and Reynolds stress agree reasonably well with experimental data.

Nomenclature

A	=	area of the space-time element interface
A^+	=	Wall model constant
C_s, C_I	=	constants for the Smagorinsky subgrid-scale model
e	=	total energy, defined in the second section
$\overrightarrow{e_x}$, $\overrightarrow{e_y}$, $\overrightarrow{e_z}$, and $\overrightarrow{e_t}$	=	unit vectors along the x-, y-, z-, and t- directions
$\boldsymbol{F}_1, \boldsymbol{F}_2, \boldsymbol{F}_3$	=	flux vectors for general conservation laws in three spatial directions
$\boldsymbol{G}$	=	source vector for general conservation laws
$\vec{\boldsymbol{h}}$	=	flux density vector in the joint space-time domain
k	=	thermal conductivity
$L_{ij}, M_{ij}, \beta, \alpha$	=	tensors used in Germano's identity
M	=	freestream Mach number

[1] Aerospace Technologist, Computational AeroSciences Branch, Email: Chau-Lyan.Chang@nasa.gov, Associate Fellow, AIAA
[2] Research Engineer, Email: balaji.s.venkatachari@nasa.gov, Senior member, AIAA

$\vec{n}$	=	unit surface normal
p	=	pressure
Re	=	Reynolds number based on a prescribe normalization length
Re_θ	=	Reynolds number based on momentum thickness
$\vec{s}$	=	surface normal vector in the joint space-time domain
t	=	time
T	=	temperature
τ	=	shear stress
u	=	streamwise velocity
$\boldsymbol{U}$	=	dependent solution vector
v	=	wall-normal velocity
V	=	integration space-time volume
$\vec{V}$	=	total velocity vector
w	=	spanwise velocity
x	=	streamwise coordinate
y	=	wall-normal coordinate
z	=	spanwise coordinate in direction parallel to leading edge
x_0, y_0, z_0	=	coordinates of solution point within the solution element
γ	=	ratio of the specific heat
δ	=	Kronecker delta
ρ	=	density
θ	=	momentum thickness
μ, λ	=	first and second coefficients of molecular viscosity
$\tilde{\mu}, \tilde{k}$	=	turbulent eddy viscosity and conductivity
$\tilde{\nu}$	=	turbulent variable for the SA model
Δ	=	filter width for subgrid-scale models
Ω	=	general surface in the space-time domain

Subscripts

x, y, z, t	=	derivatives in spatial and temporal directions
$1,2,3$	=	spatial directions along x, y, and z, respectively
∞	=	free-stream conditions
i,j,k	=	directional indices

I. Introduction

Computational fluid dynamics has become an essential tool for aerodynamic design and many fluid-dynamic related engineering product development programs. Reynolds-Averaged Navier-Stokes (RANS) computations for viscous flows across speed regimes are routinely used for steady-state configurations, targeting either design/optimization or off-design concept validations. Turbulent flows in these applications are dealt with by incorporating turbulence models to calculate the mean state. RANS models have been tuned and optimized for many such applications and the predicted mean states match reasonably well with experimental measurements, not only surface pressure/skin friction but also Reynolds stress profiles. The success stories as well as current outstanding problems are summarized on the NASA turbulence modeling resource (TMR) website (https://turbmodels.larc.nasa.gov/index.html).

Due to wide availability of large-scale computing facilities in recent years, large-eddy simulations (LES) or hybrid RANS/LES simulations [1-3] (e.g., detached eddy simulations, DES) have gained popularity, especially for problems involving separated boundary layers or highly unsteady mean motions, where the traditional RANS approach often fails to provide acceptable level of predictive accuracy. In the LES simulations, typically an underresolved mesh from the standpoint of Kolmogorov's scale is used and the small-scale contributions are accounted for either by using the intrinsic numerical dissipation (implicit LES) or by a subgrid-scale model. Large (and thus more resolvable) eddies or waves in these eddy-resolving simulations are handled by higher accuracy, lower dissipation numerical schemes. In the hybrid RANS/LES approach, closer to the wall, the RANS model is applied for attached boundary layers. Away from the wall, the model is tuned to play a diminishing role in the simulations. In the dynamic subgrid scale (SGS) model approach, a model that adapts to the filtered solution dynamically is active everywhere in the domain. The resolution of the small scales very near the wall is automatically guaranteed if the mesh is fine enough or else relies on a wall model to avoid enormous grid counts. The key ingredient of both approaches is to model only the regions where the state-of-the-art RANS type modes are mimicking realistic flow physics. The bulk of these LES computations have been carried out with either structured or unstructured hexahedral meshes, despite the fact that a tetrahedral mesh would be more suited for SGS models due to its isotropy and lack of a fixed orientation. More research is needed to understand the dynamic behavior of existing SGS models in a more isotropic tetrahedral mesh for turbulence simulations.

The other important and not yet fully understood aspect in LES is the interaction of turbulent structures with flow discontinuities. The existence of shocks makes the eddy-resolving simulations much more challenging due to unsteady interaction of all turbulent scales with the shock. An ideal shock-capturing scheme applies just enough damping to prevent numerical instability, while preserving accurate unsteady Rankine-Hugoniot jumps for all crossing eddies. A typical canonical problem is the interaction of isotropic turbulence with a normal shock. From the standpoint of LES or hybrid RANS/LES, both the large and small scales have to be accounted for reasonably well across the shock. The former is in general taken care of by the numerics alone [4-6]. Reducing numerical dissipation as well as increasing grid resolution near the shock can enhance solution accuracy. If no model is present, both small and large scales across the shock are naturally influenced by the shock capturing scheme. However, most shock capturing schemes tend to just dissipate small scales. It is still an open question as to how the subgrid scale model should be treated when a shock is presented. Additionally, turbulence interaction with the shocks gets amplified and distorted, resulting in high anisotropy, calling for the need for compressible subgrid scale models that don't rely upon local isotropy assumptions. Research along this line is currently being pursued [7]. When the shock impinges on the turbulent boundary layer directly, the interaction results in a separation region, which can further intensify the fluctuating turbulent eddies substantially. The interaction of turbulent eddies takes place through a series of compression fans, instead of a strong discontinuity. In such a scenario, the numerical dissipation requirements of the shock capturing scheme is not as stringent as the normal shock problem discussed above. On this topic of shock/turbulent boundary layer interaction, both experimental and numerical investigations have been actively pursued for decades [8-9]. Most computational investigations on this topic (e.g., Refs. [10-11]) use structured meshes with either low-dissipation second-order or high-order WENO or finite-difference schemes. Some investigations using low-dissipative unstructured mesh schemes have also emerged in recent years [12-13].

The main objective of this research is to use the emerging space-time conservation element, solution element (CESE) numerical framework [14-16] and the recently implemented dynamic modeled LES capabilities with a simplified wall model to study the behavior of SGS models in isotropic turbulence decay and to investigate interactions of turbulent boundary layer and shocks using unstructured meshes. The main advantage of a tetrahedral mesh is that it can be easily adapted to complex geometrical configurations and allows for relatively easy local refinement near critical regions. In the past, the use of tetrahedral meshes along with the popular DSM has not been actively pursued in the literature due to numerical accuracy considerations. The goal of this paper is to advance the state-of-the-art for LES predictions of supersonic turbulent flows using entirely tetrahedral meshes with good accuracy. As part of this work, the canonical problem of compressible isotropic turbulence decay is first investigated with a dynamic Smagorinsky subgrid scale model. The effectiveness of the model and its effect on eddy viscosity are assessed. Preliminary results for a high Reynolds number Mach 2.85 turbulent flow over a 30° ramp, a RANS benchmark case with experimental data from the TMR website, are computed by current wall-modeled LES simulations with a relatively coarse grid near the wall. Mean turbulent quantities are compared with experimental data and DNS results with a special focus on the backscattering of modeled scales to the large scales by the dynamic model.

II. Numerical Formulations

A. The CESE Method

The space-time conservative CESE method attempts to obtain the discretized solutions by enforcing conservation laws across the space-time computational domain. To this end, let (a) x, y, and z be the spatial coordinates, and t be the time coordinate; (b) $x_1 \stackrel{\text{def}}{=} x,\ x_2 \stackrel{\text{def}}{=} y,\ x_3 \stackrel{\text{def}}{=} z$, and $x_4 \stackrel{\text{def}}{=} t$ be the coordinates of a four-dimensional Euclidean space E_4; (c) $\overrightarrow{e_x}$, $\overrightarrow{e_y}$, $\overrightarrow{e_z}$, and $\overrightarrow{e_t}$ be the unit vectors along the x-, y-, z-, and t- directions in the 4-dimensional space, respectively; and (d) $\vec{\boldsymbol{h}}$, be the space-time flux density vector. Then $\vec{\boldsymbol{h}}$ can be expressed as

$$\vec{\boldsymbol{h}} = \boldsymbol{U}\,\overrightarrow{e_t} + \boldsymbol{F_1}\,\overrightarrow{e_x} + \boldsymbol{F_2}\,\overrightarrow{e_y} + \boldsymbol{F_3}\,\overrightarrow{e_z}, \tag{1}$$

where (a) $\boldsymbol{U}$ represents the dependent conservative variables per unit spatial fluid volume; (b) each of $\boldsymbol{F}_1, \boldsymbol{F}_2$, and $\boldsymbol{F}_3$ represents the flux functions in the three spatial directions that are differentiable functions of $\boldsymbol{U}$ and/or its spatial derivatives in some cases; and (c) $\vec{h}$ implies a tensor quantity such that a dot product with any of the unit vectors in the space-time domain results in a flux vector representing all the conserved quantities. Then, the most fundamental and general form of the unsteady conservations laws applied over a space-time flow domain D in E_4 can be cast into the following space-time unity integral form:

$$\oint_{\Omega} \vec{\boldsymbol{h}} \cdot d\vec{s} = \int_V \boldsymbol{G} dV, \tag{2}$$

where the space-time flux vector is integrated over the surface Ω of an arbitrary space-time domain V in D. The space-time surface area vector is defined as $d\vec{s} = \vec{n} dA$ where $\vec{n}$ is the outward surface unit normal and dA is the space-time surface area increment in Ω. Note that area and volume here refer to general area and volume in the space-time domain in four dimensions. One of the dimensions in these definitions could involve the increment in time. The vector $\boldsymbol{G}$ is associated with possible source terms such as body force, chemical reaction, or other external forcing. For three-dimensional compressible Navier-Stokes equations, the dependent variables are defined by $\boldsymbol{U} = (\rho, \rho u_1, \rho u_2, \rho u_3, e)^T$ where ρ, u_1, u_2, u_3, and e represents density, three velocity components, and total energy per unit volume ($e = \frac{p}{\gamma - 1} + \frac{\rho}{2}(u_1^2 + u_2^2 + u_3^2)$), respectively. Flux vectors $\boldsymbol{F}_1$, $\boldsymbol{F}_2$, and $\boldsymbol{F}_3$, contain five elements to represent mass, three momentums, and energy conservation in the spatial coordinate x, y, and z, respectively. For compressible Navier-Stokes equations, the i-th flux vector function can be expressed as

$$\boldsymbol{F_i} = \begin{pmatrix} \rho u_i \\ \rho u_i u_1 + p\delta_{i1} - \tau_{i1} \\ \rho u_i u_2 + p\delta_{i2} - \tau_{i2} \\ \rho u_i u_3 + p\delta_{i3} - \tau_{i3} \\ (e + p)u_i - k\frac{\partial T}{\partial x_i} - \tau_{ij} u_j \end{pmatrix} \tag{3}$$

where δ_{ij} is the Kronecker delta and k is the thermal conductivity. Assuming μ and λ are the first and second coefficient of viscosity, the viscous stress tensor is defined as

$$\tau_{ij} = \mu\left(\frac{\partial \boldsymbol{u_i}}{\partial \boldsymbol{x_j}} + \frac{\partial \boldsymbol{u_j}}{\partial \boldsymbol{x_i}}\right) + \lambda(\boldsymbol{\nabla} \cdot \vec{\boldsymbol{V}})\delta_{ij} \tag{4}$$

where $\vec{\boldsymbol{V}} = (u_1, u_2, u_3)$ is the velocity vector. When no external forcing or internal chemical reaction is present, the source vector G is zero and the governing equations reduce to

$$\oint_{\Omega} \vec{\boldsymbol{h}} \cdot d\vec{\boldsymbol{s}} = 0. \tag{5}$$

In fact, this integral equation is valid for all 3D time-accurate conservation laws without a source, not just limited to the fluid equations. For Navier-Stokes solutions, Eq. (5) holds even in the presence of shocks or other forms of interfacial or phase discontinuities, because fundamental conservation laws still apply. Thus, the integral form like Eq. (5) is preferred for numerical computations, instead of the differential form, where derivatives may cease to exist across discontinuities. Instead of seeking discretized solutions of differential equations, the CESE method is constructed based on the above integral equation.

Discretized equations of Eq. (5) for a tetrahedral element take the following form

$$\sum_{j=1}^{4} \vec{\boldsymbol{h}}_{ij} \cdot \Delta\vec{\boldsymbol{s}}_{\boldsymbol{ij}} = 0, \quad i = 1, \ldots, N. \tag{6}$$

In the CESE method, the individual space-time volume elements over which the space-time flux conservation is enforced is called as the conservation element (CE) and its boundaries are part of what is denoted as a solution element (SE). Thereby, in Eq. (6), the index i corresponds to one of N CEs that make up the computational domain. For a tetrahedral element, there are: (i) a total of four neighboring CEs; and (ii) each CE is bounded by five SEs (one corresponding to each of the elements and its four neighbors). Within the SEs the dependent variables $\boldsymbol{U}_i$ are assumed to be smooth and vary according to the Taylor series expansion,

$$\boldsymbol{U}_i(x, y, z, t) = \boldsymbol{U}_{0i} + \boldsymbol{U}_{ti}(t - t_0) + \boldsymbol{U}_{xi}(x - x_0) + \boldsymbol{U}_{yi}(y - y_0) + \boldsymbol{U}_{zi}(z - z_0) \tag{7}$$

where (x_0, y_0, z_0, t_0) is the solution point within the i-th SE defined as the centroid of all surrounding CEs. For high-order CESE schemes, Eq. (7) would contain higher (second and third for fourth-order schemes) derivatives in the Taylor series expansion. Within each SE, the flux functions ($\boldsymbol{F}_1$, $\boldsymbol{F}_2$, and $\boldsymbol{F}_3$) are uniquely defined (without any special treatment required to render the interface flux unique) as nonlinear functions of the dependent variables $\boldsymbol{U}_i$. Numerical dissipation in the CESE framework for irreversible physics are incorporated through the derivatives and their effects on conservation laws (flux vectors) are consistent with the Taylor series expansion to any order of approximations.

In traditional finite-volume methods, the smoothness assumption is enforced within the control volume and the flow variable itself is assumed to be discontinuous across the boundaries of the control volume. Consequently, at the interfaces of the control volume, flux vectors are not uniquely defined and ad-hoc approaches must be employed as approximate solutions at the interfaces. In contrast, the CESE method assumes smoothness only at the boundaries of the CE (i.e., surfaces of the CEs) where conservation laws are to be enforced in the integral form and discontinuities among all neighboring SEs and within the CEs are allowed to exist. By enforcing strong conservation of flux and dependent-variable vectors described by eq. (6) at each CE, it can be proven that local as well as global conservation in the space-time domain is strictly enforced without the need to apply any approximate Riemann solver for multidimensional flows. Therefore, the CESE method is a genuinely multidimensional scheme.

Additionally, in contrast to common CFD algorithms, in which the temporal derivative is treated separately by using finite differences and only spatial derivatives are integrated via either finite volume or Galerkin methods, the CESE method integrates the conservation laws over the entire discretized space-time domain without treating the space and time coordinates differently. Such consistent formulation offers uniform temporal and spatial solution accuracy up to the designed order. For flow simulations, the conservation in both space and time has the potential to improve the temporal accuracy. More details of the numerical formulation used here can be found in Refs. [14-16].

B. Large-Eddy Simulation with a Subgrid-Scale Model

RANS computations have been widely used to obtain the turbulent mean state for high Reynolds numbers flows due to its simplicity and less-demanding computing power requirements as compared to other higher fidelity methods. The governing equations for unsteady RANS take a similar form as Eq. (5), except that each flow variable represents the mean turbulent state and the viscous stress tensor now consists of two parts: a) the laminar stress as defined in Eq. (4), and b) Reynolds stress as an outcome of turbulent fluctuations. For the compressible Navier-Stokes equations, a Favre average is normally used to derive the RANS equations, details of the governing equations can be found in the literature [17-19]. The turbulent viscosity and thermal conductivity are replaced by

$$\tilde{\mu} = \mu + \mu_T \tag{8}$$

$$\tilde{k} = \mu / Pr + \mu_T / Pr_T \tag{9}$$

where Pr and Pr_T are the laminar and turbulent Prandtl numbers, respectively, and μ_T is the eddy viscosity. The turbulent eddy viscosity needs to be modeled by either employing simple phenomenological estimations or by more complex differential equations. To date, most successful models are based on some form of differential equation derived by physical reasoning and perhaps more heavily, by empirical observations through trial and error. The CESE method is formulated by the integral form of the conservation laws and the solutions of the discretized equation, Eq. (6), ensures that the imposed turbulent stresses satisfy conservation laws for each conservation element as well as the entire computational domain. It can be thus argued that, the best turbulence model for the CESE method is likely to be a set of Reynolds stress models that incorporate the additional turbulence fluctuation contributions to the three momentums and the total energy conservation laws over all integrated CEs. Discussion of RANS computations using the CESE method is outside the scope of this paper. Here, it is noted that for flat plate boundary layers, the RANS results using the CESE method show good agreement with existing solutions from the literature [34].

For LES, subgrid-scale models are typically derived for the spatially filtered Navier-Stokes equations. By assuming a prescribed filter width and using the Favre average, the Navier-Stokes equations can be written for the filtered variables in a form similar to Eqs. (3)-(5), except for the additional subgrid scale shear stress tensor and a few relatively less important, albeit case-dependent, extra terms in the energy equations [1, 20-21]. In the original Smagorinsky model [22], the filtered equations are solved by modeling the subgrid shear stress as,

$$\tau_{ij} - \frac{\delta_{ij}}{3}\tau_{kk} = -2C_s\bar{\rho}\Delta^2|\tilde{S}|\left(\tilde{S}_{ij} - \frac{\delta_{ij}}{3}\tilde{S}_{kk}\right), \qquad \tau_{kk} = 2C_I\bar{\rho}\Delta^2|\tilde{S}|^2 \tag{10}$$

where $\tilde{S} = \sqrt{2S_{ij}S_{ij}}$ is the filtered strain rate tensor magnitude and Δ is the filter width. The subgrid-scale heat flux can be evaluated accordingly by assuming a constant turbulent Prandtl number. Smagorinsky [22] suggested constant values of $C_s = 0.16$ and $C_I = 0.09$.

The original Smagorinsky model discussed above lacks the dynamic features of interactions between resolved and subgrid-scale eddies. Moin et al. [2] proposed a dynamic Smagorinsky model that allows the coefficients of the subgrid-scale model to be adjusted actively based on the instantaneous filtered solutions. The following coefficients are derived by the Germano identity [23],

$$C_s\Delta^2 = \frac{1}{2}\frac{<L_{ij}M_{ji}>}{<M_{ij}M_{ji}>}, \qquad C_I\Delta^2 = \frac{1}{2}\frac{<L_{kk}>}{<\beta - \hat{\alpha}>} \tag{11}$$

where L and M are tensors representing differences in filtered solutions and quantities β and $\hat{\alpha}$ are two different products of filtered strain rate magnitudes. Definitions of these quantities can be found in Refs. [20-21, 23]. The operation $<\cdot>$ denotes the spatial average over the homogeneous flow direction. For example, the spanwise direction for a 2D boundary layer can be regarded as the homogenous direction. For unstructured mesh simulations, however, calculating the spatial average along the homogeneous direction appears to be nontrivial. Furthermore, in many complex flows, there is no discernible direction along which spatial averages could be computed. In this study, this operation is replaced by a test filter operation carried out by volume-averaging around all neighbors of the given solution element. This approach was suggested in Refs. [21, 24]. For unstructured-mesh LES, an additional subgrid-scale kinetic energy equation is sometimes incorporated to more accurately capture nonequilibrium turbulence effects [24] or to improve accuracy associated with pressure dilatation effects for compressible flows [21]. This additional equation along with extra terms in the energy equation discussed in Ref. [20] are not implemented in the present study.

The dynamic model has been widely used in jet and shear layer turbulent simulations for decades [1]. For wall-bounded flows, the requirements to resolve near wall eddies still render the LES too expensive for large Reynolds number boundary layers. The remedy is to impose either a RANS model or an equilibrium model near the wall region while the rest of the domain is computed with either an SGS model or without any model at all (e.g., Refs. [3, 25,26]). There has been renewed interests in applying wall models to high Reynolds number boundary layers in recent years, mainly as an alternative to resolve turbulent separation more accurately than the state-of-the-art RANS models. Nonequilibrium wall models [27] are also being attempted, although only limited success has been reported for subsonic flows. In this paper, a simplified wall model is proposed. The dynamic Smagorinsky model is applied everywhere in the domain except at a layer very near the wall. For unstructured meshes, the “first” wall layer is defined as all elements that are in direct contact with the viscous wall either by vertices or faces. The second layer is thus those elements in direct contact with the first wall layer. Within a predetermined wall layer, a RANS-like model is applied, namely, the eddy viscosity is computed using the mixing length model,

$$\mu_t = \kappa \mu_w y^+ \left[1 - exp\left(\frac{y^+}{A^+}\right)\right]^2 \tag{12}$$

where $\kappa = 0.41$ and $A^+ = 26$. Molecular viscosity at the wall is denoted by μ_w and turbulent wall-normal distance by y^+. Turbulent Reynolds stresses are computed using the above eddy viscosity for the wall layer. The communication of these additional stresses with the subgrid scale models is via the conservation laws. In other words, the computed subgrid-scale stress near the wall is to be matched to a prescribed wall stress based on the mixing length model. In contrast to the usual equilibrium model, the eddy viscosity equation is not used to solve the variation near the wall. The turbulent y^+ of the first layer should be set such that it is large enough to make high-Reynolds number simulations feasible but not too large to affect the near wall dynamics. Its value is purely empirical, a y^+ of 10 to 50 has been tested for a Mach 2.9 flow over a 24° ramp. It appears that this value decreases as the Reynolds number increases. When the first layer thickness decreases, the wall model effect diminishes, and the solution approaches that without a wall model.

An alternative for RANS-based wall-modeled LES is to apply a slip-wall model, as suggested by Bose and Moin [28]. In this approach, a slip-wall equation for the filtered velocity and its gradient is derived by applying the known Green’s function in the incompressible limit. Coupling with the near-wall Reynolds stress equation, one can solve for the filter width, velocity gradient, and slip-wall velocity at the near wall element without needing to resolve the near wall regions. The formulation has the advantages of being free of adjustable constants and automatically reverting back to no-slip conditions in the separated region. Unfortunately, a working formulation for compressible flows is not yet available. In this research, as an initial step to assess the effectiveness of the implemented SGS models for high Reynolds number turbulent boundary layers, an analogous slip-wall model is implemented by employing symmetry conditions for scalar dependent variables and antisymmetry for the velocity vector using the wall boundary as a mirror. The resulting filtered velocity and its gradients at the wall boundary are imposed as the slip-wall condition. The filter width (cubic root of the averaged surrounding control volumes) for the near wall element is calculated by one-sided averaging without factoring in the symmetry conditions. In the separated region for the shock boundary layer interaction case to be presented later, the same slip-wall conditions are applied, even though theoretically, one can revert back to no-slip conditions.

III. Results

To-date, most LES investigations using DSM have been with both structured and unstructured hexahedral meshes. Numerical schemes used in these computations are derived by employing the method of lines (MOL), i.e., discretization of partial differential equations, and flux conservation is only applied to spatial derivatives, resulting in an ordinary differential equation in time. This derivation offers flexibility for various kinds of time integrators including implicit schemes for steady state solutions. However, its effects on temporal accuracy have not yet been formally and systematically assessed. The space-time CESE method solves the governing Navier-Stokes equations by enforcing flux conservation in all four dimensions simultaneously. As pointed out in Ref. [29], after comparing various MOL finite-volume approaches (which are the baseline formulations for most of LES available in the literature) with the space-time CESE method, only the latter approach correctly predicts crystal growth in a dispersed system dominated by convection. In this paper, the impact of non-MOL numerical schemes such as the CESE method, on subgrid scale modeling in turbulence simulations is assessed for the first time by studying the dynamic variation of the subgrid-scale eddy viscosity predicted by the DSM. Two canonical problems are investigated: a) decay of compressible isotropic turbulence and b) shock turbulent boundary layer interaction over a ramp. This paper focuses on the overall evaluation of the SGS model in resolving the eddies away from the very near wall layer, not the equilibrium/nonequilibrium or slip wall models. For this reason, only approximated wall models, as described in the previous section, are used in conjunction with a relatively coarse near wall mesh in the order of $\Delta y^{+} = 10$. No rigorous grid refinement study, except for the isotropic turbulence decay simulations, is intended in this paper.

A. Backscattering in Compressible Isotropic Turbulence Decay

Decay of compressible isotropic turbulence at a turbulent Mach number of 0.6 is simulated both with (only for four coarser grids) and without (for all five levels of grids) using the dynamic SGS model described above. The turbulent kinetic energy spectra after the flow has evolved four times the Taylor time scale are shown in Fig. 1 for several grids over a periodic box of $(2\pi)^3$. The tetrahedral mesh size has been converted to an equivalent structured mesh size by taking the cubic root of the total number of elements. Detailed direct simulation (no model) results using the CESE method along with comparisons with very fine grid DNS solutions from the literature can be found in Ref. [30]. The addition of DSM appears to have slightly increased damping effects on the high wave number components and very minimal effects are observed on larger scale (low wave numbers), as expected. The addition of the DSM does not appear to help resolve small scale turbulence for this canonical problem because the turbulent structure is indeed decaying and no *net* back scattering is supposed to take place for a uniform mean flow. This slight damping effect has also been observed by other investigations [2]. In general, the use of subgrid-scale models does not seem to improve the overall resolution for this canonical problem. However, it offers a means to evaluate the backscattering effects in isotropic turbulence simulations, as will be discussed below.

One of the main objectives of using a dynamic model in the LES is its capability to model backscattering, namely, the energy propagation from the small subgrid scales to the larger, resolved scales. This can be realized better by inspecting the sign of the dynamic coefficients C_s in Eq. (11). As designed, the coefficient C_s can be either positive or negative. A negative coefficient implies negative eddy viscosity, which allows for backscattering of energy. Nonetheless, in most DSM calculations, if not all, an ad-hoc clipping procedure to avoid numerical instability associated with negative viscosity is employed (see for instance, Ref. [1, 31]). In Ref. [32], it was pointed out that accounting for backscattering is essential in LES of transitional flows. Furthermore, by analyzing the DNS data of turbulence channel flows and compressible isotropic turbulence decay, it was found that the portion of grid points in the DNS where backscattering occurs can be as large as 50%. It is apparent that a pure dissipative SGS model in the LES cannot predict the correct physics, especially if the backscattering process is limited for the sake of numerical stability.

The current results with tetrahedral meshes and space-time flux conservation formulations show no issues associated with negative eddy viscosity for isotropic turbulence decay as well as shock/turbulent boundary layer simulations to be discussed later. No tripping or limiting needs to be applied for the computed instantaneous eddy viscosity. Possible reasons for this much more numerically stable behavior, in addition to non-MOL space time flux conservation, are perhaps related to the more consistent relationship between the physical fluxes and the dependent variable polynomials that are free of any reconstructions at the cell interfaces. Figure 2 shows the negative eddy viscosity distribution computed by the subgrid-scale model for four different grids. The overall eddy viscosity decreases as the grid is refined. Although hard to be discerned from the current scale in Fig. 2, the peak values in both cases are located on the positive eddy viscosity side (for instance, 0.04 and 0.013 for 64^3 and 96^3 grids, respectively), due to the overall decaying trend of turbulent structures in this particular problem. The trend with increasing resolution also complies with flow physics in that with an increasing resolution, the distribution should become sharper and sharper and eventually approach a delta function at a small positive value for infinite grid resolution. Figure 3 compares several selected negative eddy viscosity isosurfaces for two coarse grid cases. The volume percentage of backscattering is 38.3%, 38.8%, and 39.3% for the 64^3 , 96^3, and 128^3 grids, respectively. This appears to be in line with the values in Ref. [32] computed from DNS data, where it varies from 50% for a small amount of grid filtering to about 40% for large filtering.

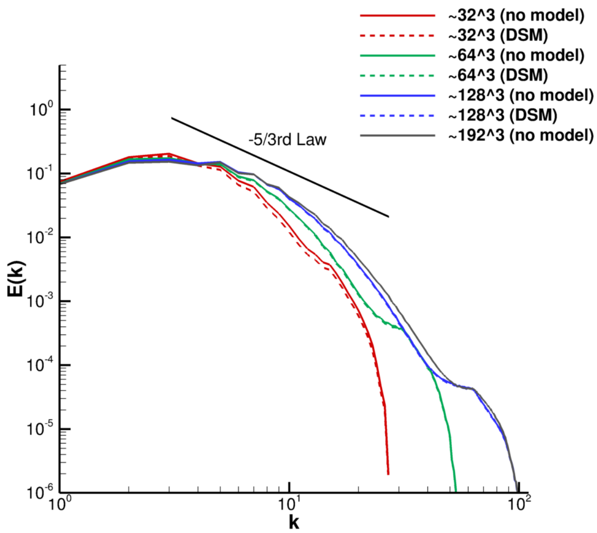

Figure 1. Isotropic turbulence decay simulated with and without the subgrid scale DSM, showing turbulent kinetic energy spectra after 4 Taylor time scales for four different meshes.

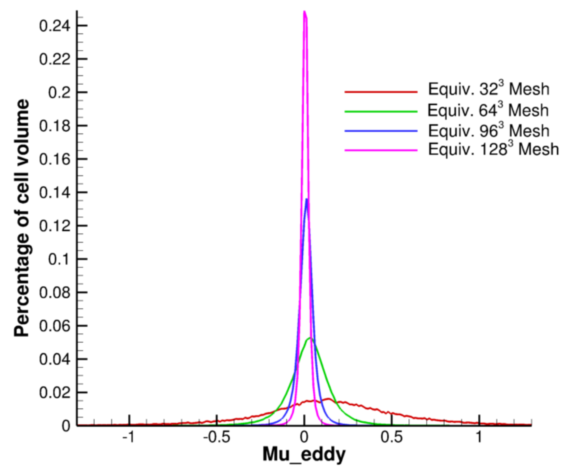

Figure 2. Percentage of cell volumes versus instantaneous eddy viscosity (normalized by free-stream viscosity) predicted by the subgrid-scale model for four different grids.

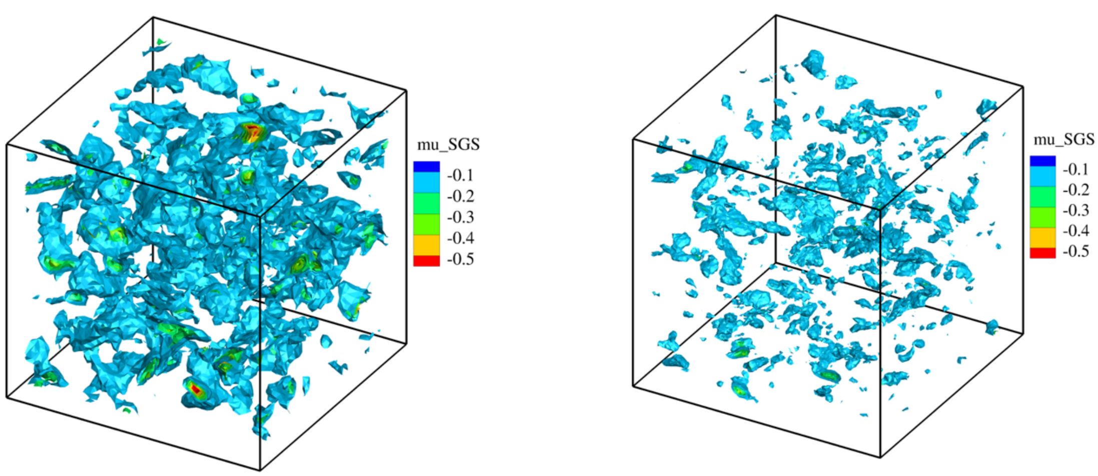

(a) (b)

Figure 3. Isosurfaces of instantaneous negative eddy viscosity for isotropic turbulence decay, showing backscattering with two different grids: (a) 64^3 equivalent tetrahedrons (b) 128^3 equivalent tetrahedrons

B. Shock Turbulent Boundary-Layer Interaction at Low Reynolds Number

The approximated wall-model approach by imposing eddy viscosity at near wall layers using Eq. (12) is tested for Bookey's turbulent boundary layer interaction problem [9]. The flow is a Mach 2.9 supersonic turbulent boundary layer past a 24° compression corner with a momentum thickness Reynolds number of $Re_\theta = 2400$. This relatively low Reynolds number problem has been investigated using DNS by several groups (e.g., Refs. [11, 30]). A coarse near wall grid with $\Delta y^+ = 50$ (with $\Delta x^+ = \Delta z^+ = 64$) is used in the LES simulation (total of 9.6 million tetrahedrons) with the dynamic model. Results are compared with DNS (using 45 million tetrahedral elements with a near wall grid of $\Delta y^+ = 0.2$) and experimental data in Fig. 4 where mean wall pressure distribution along the ramp and mean streamwise velocity profiles depicted at four times the initial boundary layer thickness downstream of the corner are shown. As can be seen, the LES results are in reasonably good agreement with the DNS results at a fraction of the cost. The discrepancy in the mean velocity profile shown in Fig. 4(b) is the largest near wall. This is in part due to a large near wall spacing. Solving an additional differential equation, as was done in most equilibrium model LES (e.g., [26]), near the first layer would help resolve this region much better. The goal of this investigation is not to repeat wall modeled LES using the current LES implementation, but rather, to demonstrate that the DSM is able to resolve most of the flowfield properly with a coarser than DNS grid at such a relatively low Reynolds number. It is noted that the most gain in efficiency for this LES simulation is associated with a much larger time step used in time marching, which is determined by the smallest grid spacing in the domain for explicit schemes.

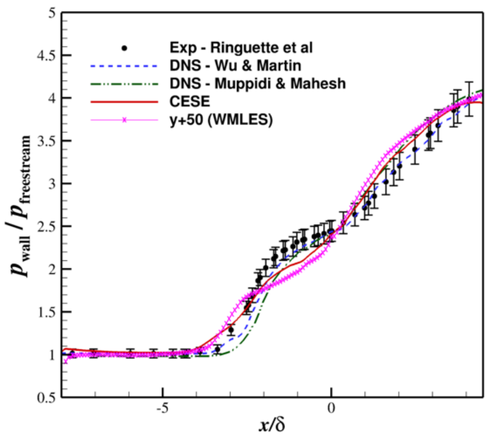

(a)

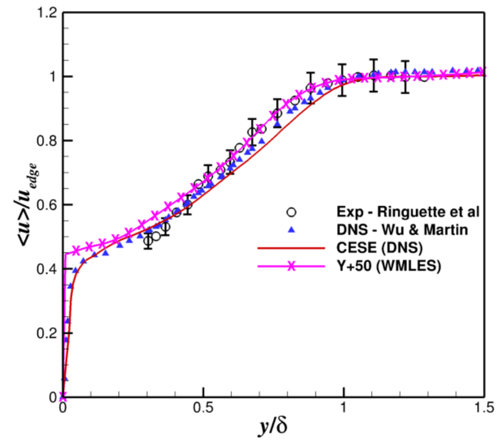

(b)

Figure 4. Comparison of wall-modeled LES and DNS results for Bookey's experiments [9] : (a) mean wall pressure distribution along the ramp (b) mean streamwise velocity distribution at four times the initial boundary layer thickness downstream of the corner.

C. Shock Turbulent Boundary-Layer Interaction at High Reynolds Number

A supersonic turbulent boundary layer over a compression cone-flare is selected as the other benchmark problem for the assessment of the SGS and wall models implemented. The standard NASA high Reynolds number shock wave boundary layer interaction case described on the TMR website computed by the current LES approach with a slip-wall model is reported in this section. Due to the lack of a differential equation-based wall model in the current implementation, the combination of SGS and an equilibrium wall model approach (see [35]) is not tested in this paper. The case is a Mach 2.85 flow over a cylindrical 30° cone flare with a one inch base radius before the corner. Experimental measurements are available from Ref. [33]. The exact Reynolds number at the corner is unknown from the experiments due to uncertainties, but is estimated to be around 1.1×10^7. To roughly match the experimentally measured boundary layer thickness at the inflow boundary of the LES domain located 10 cm from the corner, 2D RANS computations were carried out at the experimental conditions and the inflow profiles were extracted at about $Re_x = 8.6 \times 10^6$ with a boundary layer thickness of about 9 mm.

Similar to Ref. [30], the instantaneous inflow turbulent boundary layer was precomputed by the recycling approach via fixing the turbulent mean states in a smaller domain that extends $5\delta \times 9\delta \times 3\delta$ along the streamwise, wall-normal, and spanwise directions, respectively. For supersonic turbulent inflow generation using the recycling/rescaling approach, a streamwise width of 3-5 boundary-layer thickness is typically used in the literature (e.g., Refs. [11,30]). As a first assessment, the curvature effect is neglected in the recycling computations. Several wall-normal grid resolutions were tested. The minimum resolution required to maintain a turbulent motion during the recycling simulations appears to be around $\Delta y^+ = 20$ at the given Reynolds number, based on the rms level predicted. Figure 5 summarizes the predicted eddy viscosity distribution over the domain. As can be seen in Fig. 5(a), alternating positive and negative eddy viscosities are present throughout the domain. The percentage of volume distribution for three grids in Fig. 5(b) show a clear convergent trend from $\Delta y^+ = 30$ to $\Delta y^+ = 20$, but not for further refinement to $\Delta y^+ = 10$. Similar to the isotropic case presented above, the dynamically computed eddy viscosity varies from negative to positive values throughout the domain. Counting within 2 boundary layer thicknesses from the wall, typically 40.5% of cell volumes possess negative eddy viscosity, indicating backscattering. For comparison, it was reported in Ref. [32] that this ratio varies from 50% to 20% for channel flows and is a function of Reynolds number.

The LES mesh for the entire cone-flare extends from 10 cm upstream of the corner until roughly the end of the experimental configuration. The wall-normal height (9δ) and spanwise width (3δ) remain the same as the recycling domain. Four different meshes were used for the LES simulations. The first three are planar geometries, which neglect the curvature effect with three different mesh spacings near the wall: P1) $\Delta x^+ = 72,\ \Delta y^+ = 10,$ P2) $\Delta x^+ = 72,\ \Delta y^+ = 20$, and P3) $\Delta x^+ = 36,\ \Delta y^+ = 20$. The spanwise spacing is $\Delta z^+ = 50$ for all three meshes. A structured hexahedral mesh was generated for each case and then sliced to tetrahedral meshes by following the same direction except for places where mesh connectivity dictates orientations. Thus, more elements are generated along each spatial direction as compared to the corresponding structured mesh counterpart. This results in 15.6, 12.8, and 25.6 millions tetrahedral elements, respectively. The last cylindrical mesh, C1, is generated by the unstructured, advancing-front, Helden mesh generator (https://heldenaero.com/heldenmesh/) with a referencing near wall spacing of $\Delta y^+ = 20$, and $\Delta x^+ = \Delta z^+ = 70$. It should be noted that isotropic triangles are used to generate the surface mesh with the spacing in x and z indicated here, unlike the fixed spacing in a structured mesh. The spanwise domain spans around a 60° azimuthal angle. This results in a total of 12.2 million tetrahedral elements. Compared with the first three planar meshes, the last one has more random orientation and is less organized outside the boundary layer. Prestored instantaneous solutions from the recycling runs are fed into the inlet of the computational domain. Non-reflective boundary conditions are imposed at the outflow downstream of the flare. The approximated slip-wall model described in Section II is imposed at the wall and freestream conditions are applied at the top boundaries. For all three planar meshes, periodic boundary conditions are imposed at spanwise boundaries. For the cylindrical mesh, the same periodic boundary condition results in an early separation due to unknown reasons. Possible issues are the large (60°) spanwise domain or the inaccuracy of the approximated slip-wall model when applied to the cylindrical configuration. Results shown below were computed by imposing nonreflecting boundary conditions at spanwise boundaries, which gives more reasonable agreement with the solutions from the planar meshes. Turbulent statistics are gathered after 6 to 10 flow through times.

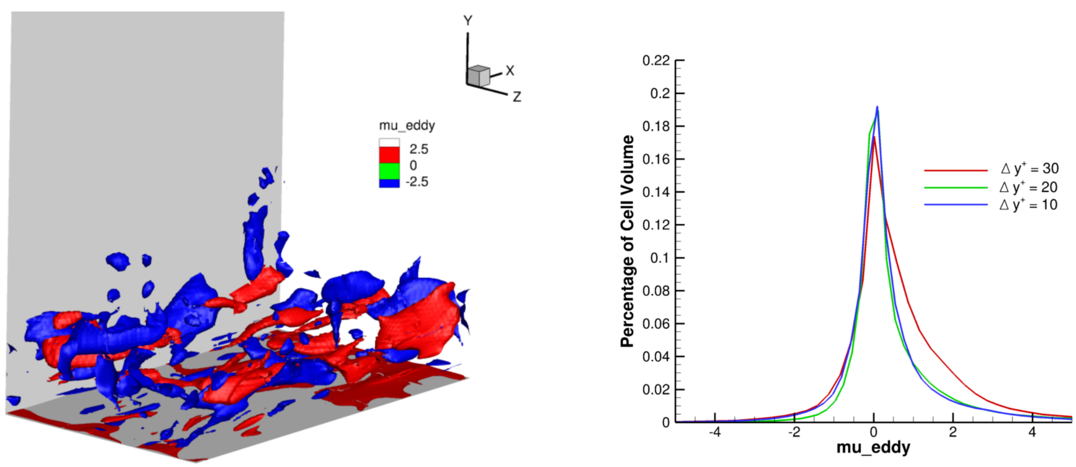

(a) (b)

Figure 5. Instantaneous eddy viscosity distribution from the recycling solution over a periodic flat plate: (a) isosurfaces of constant eddy viscosity for $\Delta y^+ = 10$ (b) percentage of cell volume distribution over a range of positive and negative eddy viscosity.

The computed turbulent eddy structures using the first planar mesh described above and the mean wall pressure from all four grids along with the experimental data are shown in Fig. 6. Table 1 summarizes the predicted separation region location and size and the comparison with experimental data. For all four meshes, the rise of wall pressure and the separation region length agree reasonably well with the data. Two planar meshes P1 and P3 give very close mean wall pressure distribution throughout but they appear to overpredict the pressure on the flare. In contrast, the cylindrical mesh results overpredict the mean pressure in the separation region but agree with the data much better on the flare portion. The nonsmooth mean pressure distribution for the C1 mesh stems from pure unstructured mesh on the surface. The spanwise averaging process for this cylindrical mesh does not smooth out the variation along the spanwise direction, unlike the other three well-organized spanwise planar grids. Mesh P2 predicts a later pressure rise and smaller separation region length as compared with the other two planar meshes. This suggests that grid refinement in either the streamwise or wall-normal direction helps resolve the separation region better. While there is no "perfect" agreement with the data in terms of the separation region, the LES predictions are in general better than the RANS predictions given on the TMR website. More computations are needed for the cylindrical mesh with spanwise periodic boundary conditions in the future to see its merits in terms of agreement with the data.

Table 1. Comparison of predicted separation region locations and length with experiments for four grids.

	Separation point (cm)	Reattach point (cm)	Length (cm)
Experiments [33]	-2.73	0.97	3.70
Planar, $\Delta y^+ = 10, \Delta x^+ = 72$ (P1)	-2.67	0.77	3.44
Planar, $\Delta y^+ = 20, \Delta x^+ = 72$ (P2)	-1.80	0.67	2.47
Planar, $\Delta y^+ = 20, \Delta x^+ = 36$ (P3)	-2.45	0.91	3.36
Cylindrical, $\Delta y^+ = 20$ (C1)	-2.27	2.16	4.43

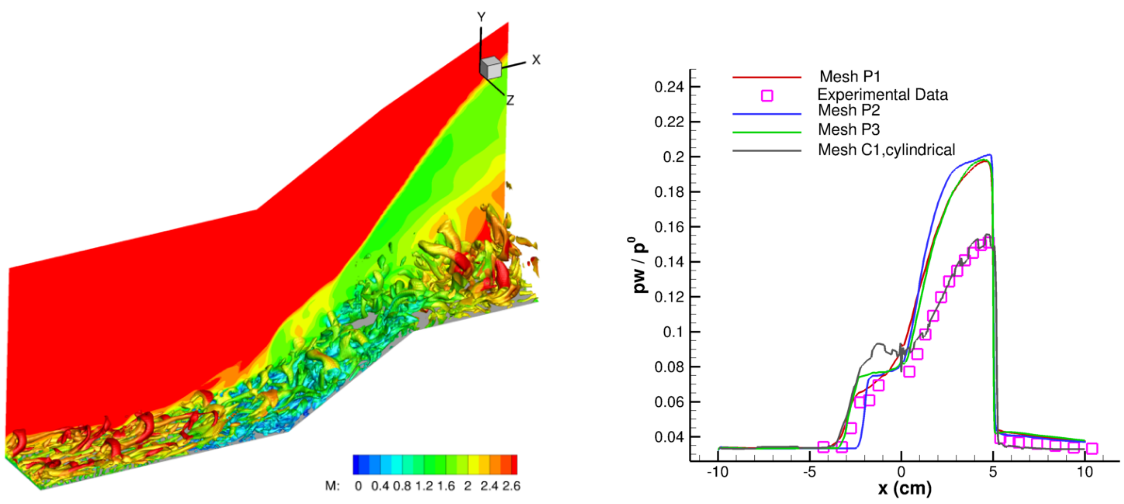

(a) (b)

Figure 6. Shock turbulent boundary layer interaction for the NASA Mach 2.85 benchmark case: (a) instantaneous Q-criterion distribution colored by Mach numbers from Mesh P1 (b) computed mean wall pressure distribution using four different grids, compared with data [33].

Figures 7-9 depict the mean streamwise velocity, wall-normal velocity and Reynolds stress distributions at selected experimentally measured locations, respectively. Only results from the first two planar meshes (excluding the more refined streamwise mesh case) and the cylindrical mesh are shown for comparison. The overall agreement is reasonable for these high Reynolds number flows using the current slip-wall-modeled LES. In general, the predicted Reynolds stress $< u'v' >$ distribution shows some improvement over typical RANS results obtained using the SA model (see the TMR website). Despite missing the peak values, similar shape and trends in the separated region from the present results are evident. Using the limited data set from the experiments, it is difficult to discern which mesh gives the best prediction. As stated earlier, the goal is to evaluate the general trend of the LES prediction, not to perform a grid refinement study for the present case. As a final note, the instantaneous eddy viscosity distribution at the center plane for the P1 mesh is shown in Figure 10. Active eddy production (negative eddy viscosity) and dissipation (positive eddy viscosity) are evident in the separation region as well as on the ramp in the LES computations, indicating the necessity of a faithful dynamic SGS model that can handle both positive and negative eddy viscosities. The results shown here also reveal that some predicted mean turbulent statistics are sensitive to different meshes. Further studies are needed to identify the source of the sensitivity.

IV. Summary

Large eddy simulations using dynamic Smagorinsky models have been carried out for the decay of compressible isotropic turbulence as well as shock wave turbulent boundary layer interactions using tetrahedral meshes. With the non-MOL CESE method that enforces strong space and time flux conservation, it was found that eddy viscosity computed with the dynamic Smagorinsky model actively varies from negative to positive values. Backscattering of energy from small, modeled scales to the larger, resolved scales is evident in all the simulations performed without any numerical issues. The volume percentage of backscattering is around 40% for the two benchmark problems investigated. Preliminary results for the NASA shock boundary layer interaction test case computed with the newly implemented wall modeled LES capability on several relatively coarse grids, with about 12-25 million tetrahedral elements and a near wall mesh of $y^+ = 10$ or $y^+ = 20$, agree reasonably well with the experimental data. Improved equilibrium or slip wall models to be implemented in the future may help improve the current LES capabilities in terms of better agreement with the experimental data.

Acknowledgments

The research funding for this research has been provided by the Revolutionary Computational AeroSciences subproject under the Transformational Tools and Technologies (TTT) project of NASA Transformative Aeronautics Concepts Program (TACP).

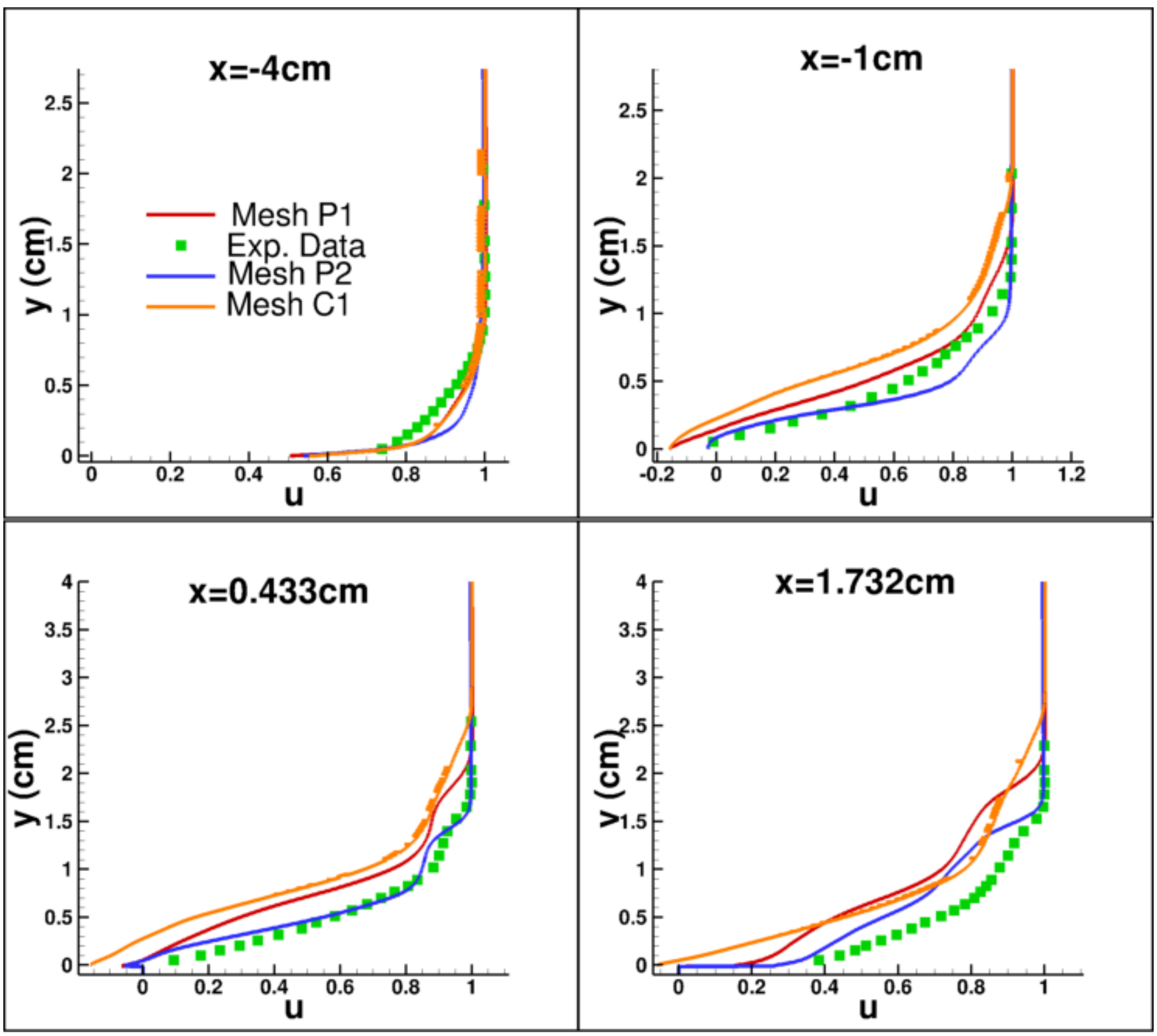

Figure 7. Predicted mean streamwise velocity distributions at four experimentally measurement locations compared with data, lines are computational results and symbols represent data[33] (x = 0 at the first corner).

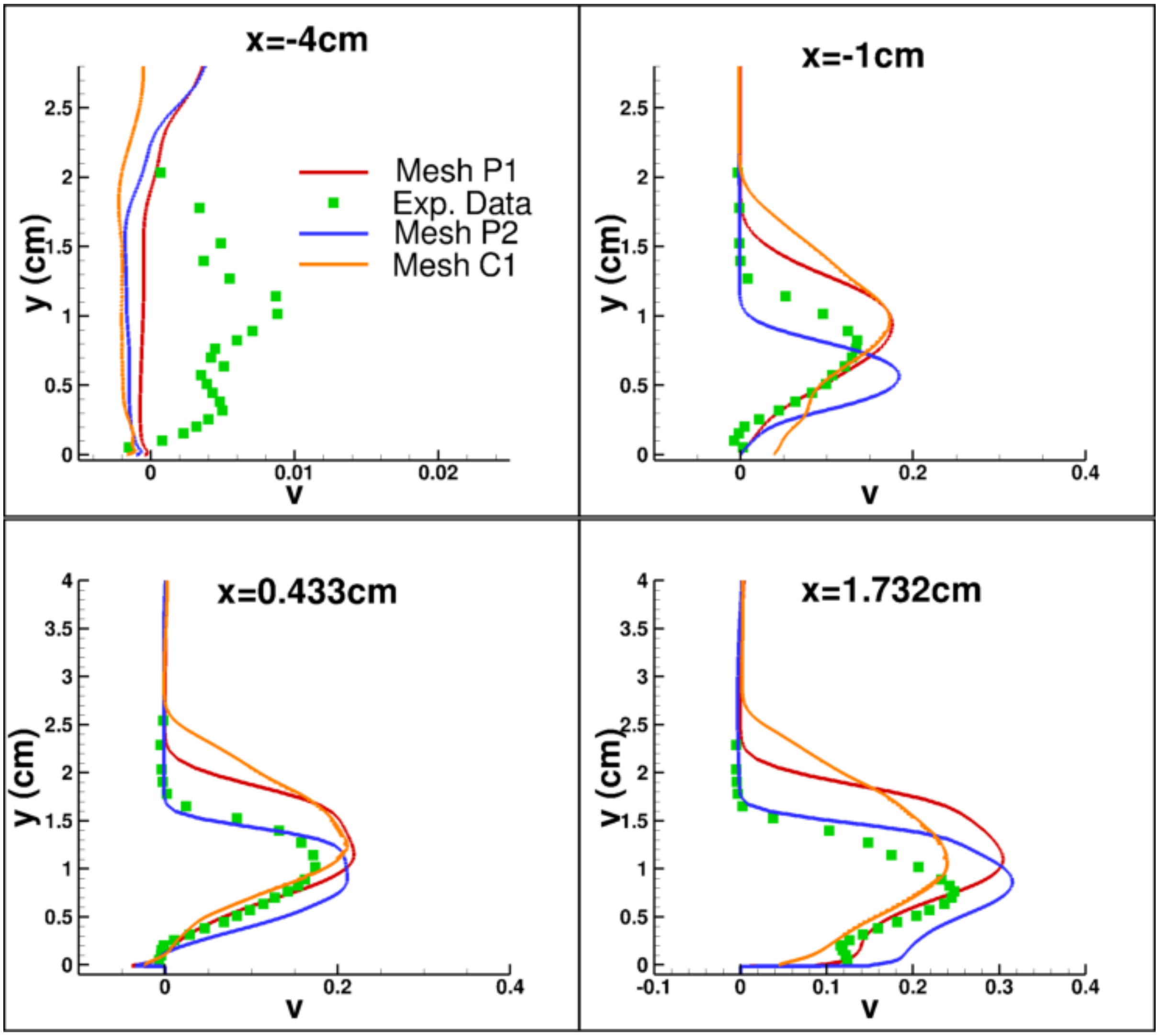

Figure 8. Predicted mean wall-normal velocity distributions at four experimentally measurement locations compared with data, lines are computational results and symbols represent data[33] (x = 0 at the first corner).

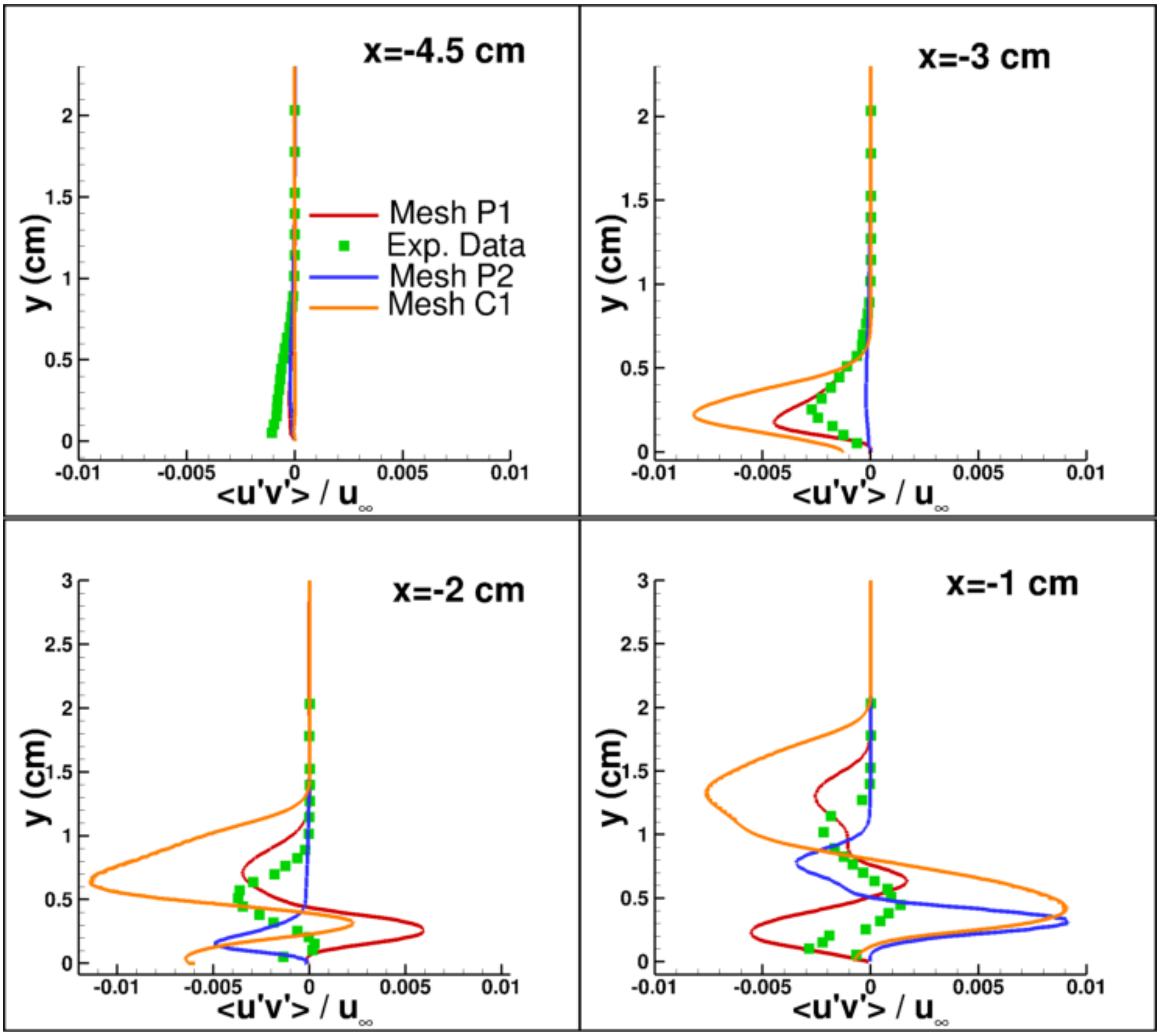

Figure 9. Predicted Reynolds stress $< u'v' >$ distributions at four experimentally measurement locations compared with data, lines are computational results and symbols represent data [33] (x = 0 at the first corner).

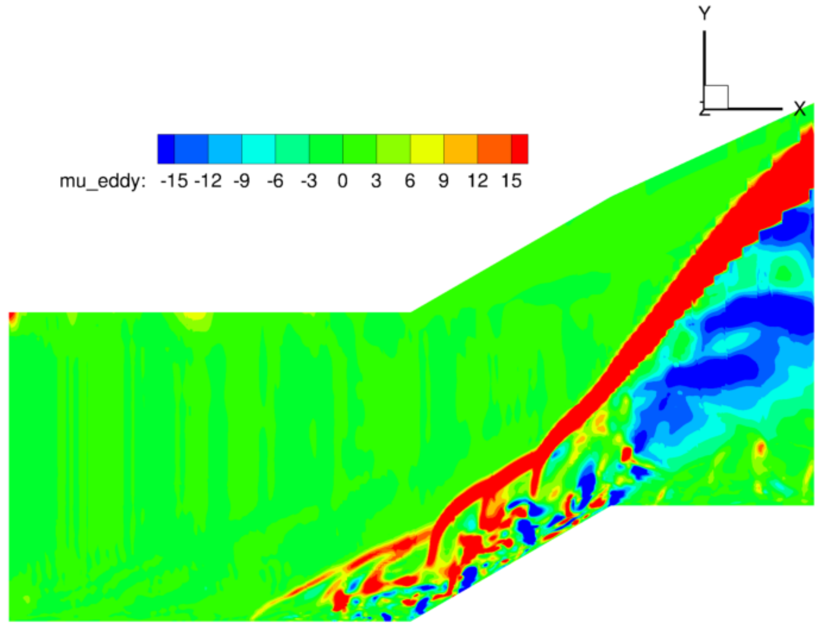

Figure 10. Instantaneous SGS eddy viscosity at the center spanwise plane obtained from solutions of P1 mesh.

References

[1] Garnier, E. Adams, N., and Sagaut, P., "Large Eddy Simulation for Compressible Flows," Springer Scientific Computation series, 2009.

[2] Moin, P., Squires, K., Cabot, W. and Lee, S., "A Dynamic Subgrid-scale Model for Compressible Turbulence and Scalar Transport," *Phys. Fluids*, **3**(11), pp. 2746-2757, 1991.

[3] Spalart, P. R., "Detached-eddy Simulation," *Annu. Rev. Fluid Mech.*, Vol. 41, pp. 181-202. 2009.

[4] Lee, S., Lele, S. K., and Moin, P., "Direct Numerical Simulation of Isotropic Turbulence Interacting with a Weak Shock Wave," *J. Fluid Mech*., Vol. 251, pp. 533–562, 1993.

[5] Lee, S., Lele, S. K., and Moin, P., "Interaction of Isotropic Turbulence Interacting with Shock Waves: Effect of Shock Strength," *J. Fluid Mech*., Vol. 340, pp. 225–247, 1997.

[6] Larsson, J., and Lele, S. K., "Direct Numerical Simulation of Canonical Shock/Turbulence Interaction," *Phys. Fluids*, Vol. 21, pp. 126101, 2009.

[7] Kotov, D. V., Yee, H. C., Wray, A. A., Hadjadj, A., and Sjogreen, B., "High Order Numerical Methods for the Dynamic SGS Model of Turbulent Flows with Shocks," AIAA Paper 2015-2297, 2015.

[8] Edwards, J. R., "Numerical Simulations of Shock//Boundary Layer Interactions Using Time-Dependent Modeling Techniques: A Survey of Recent Results," *Progress in Aerospace Sciences*, 44, pp. 447-465, 2008.

[9] Bookey, P. B., Wyckham, C., Smits, A. J., and Martin, M. P., "New Experimental Data of STBLI at DNS/LES Accessible Reynolds Numbers," AIAA Paper 2005–309, 2005.

[10] Bisek, N. J., Rizzetta, D. P., and Poggie, J., "Exploration of Plasma Control for Supersonic Turbulent Flow Over a Compression Ramp," AIAA Paper 2012-2700, 2012.

[11] Wu, M., and Martin, M. P., "Direct Numerical Simulation of Supersonic Turbulent Boundary Layer over a Compression Ramp," *AIAA J*, Vol. 45, No. 4, pp. 879–89, 2007.

[12] Muppidi, S., and Mahesh, K., "DNS of Unsteady Shock Boundary Layer Interaction," AIAA Paper 2011- 724, 2011.

[13] Khalighi, Y., Nichols, J. W., Lele, S. K., Ham, F., and Moin, P., "Unstructured Large Eddy Simulation for Prediction of Noise Issued from Turbulent Jets in Various Configurations," AIAA Paper 2011-2886, 2011.

[14] Chang, C.-L., "Three-Dimensional Navier-Stokes Calculations Using the Modified Space-Time CESE Method," AIAA Paper 2007-5818, 2007.

[15] Chang, C.-L., Venkatachari, B., and Cheng, G, "Time-Accurate Local Time Stepping and High-Order Space-Time CESE Methods for Multi-Dimensional Flows with Unstructured Meshes," AIAA Paper 2013-3069, 2013.

[16] Chang, C.-L., Venkatachari, B. S., and Cheng, G. C., "Tetrahedral-Mesh Simulation of Turbulent Flows with the Space-Time Conservative Schemes," AIAA Paper 2015-3084, 2015.

[17] Gatski, T. B. and Bonnet, J.-P., "Compressibility, Turbulence and High Speed Flow," 2009, Elsevier, Amsterdam.

[18] Wilcox, D. C., "Turbulence Modeling for CFD," 2006, DCW Industries, La Canada, CA.

[19] Hirsch, C., "Numerical Computation of Internal and External Flows, Vol. 2," 1990, John Wiley & Sons, Chichester

[20] Martin, M. P., Piomelli, U., and Candler, G. V., "Subgrid-Scale Models for Compressible Large-Eddy Simulations," *Theoret. Computational Fluid Dynamics*, Vo. 13, 2000, pp. 361-376.

[21] Park, N. and Mahesh, K., "Numerical Modeling Issues in LES of Compressible Turbulence on Unstructured Grids," AIAA Paper 2007-0722, 2007.
[22] Smagorinsky, J., "General Circulation Experiments with the Primitive Equations. I. The Basic Experiment," *Mon. Weather Rev*. Vol 91, 1963, pp.99-164.
[23] Germano, M., "Turbulence: the Filtering Approach," *J. Fluid Mech*., Vol. 238, 1992, pp. 325-336.
[24] Kim, S.-E., "Large Eddy Simulation Using an Unstructured Mesh Based Finite-Volume Solver," AIAA Paper 2004-2548, 2004.
[25] Piomelli, U. and Balaras, E., "Wall-layer Models for Large-Eddy Simulations," *Annu. Rev. Fluid Mech*. 34, 349, 2002.
[26] Larsson, J. and Kawai, "Wall-modelling in Large Eddy Simulation: Length Scales, Grid Resolution and Accuracy," Center for Turbulence Research, Annual Research Briefs, pp. 39-46, 2010.
[27] Park, G. I. and Moin, P., "An Improved Dynamic Non-equilibrium Wall-model for Large Eddy Simulation," *Phys. Fluid*, 26. 015108, 2014.
[28] Bose, S. T. and Moin, P., "A Dynamic Slip Boundary Condition for Wall-modeled Large-Eddy Simulation," *Phys. Fluid*, 26. 015104, 2014.
[29] Motz, S., Mitrovic, A., and Gilles, E.-D., "Comparison of Numerical Methods for the Simulation of Dispersed Phase Systems," *Chemical Engineering Science*, Vol. 57, pp. 4329-4344, 2002.
[30] Venkatachari, B. S. and Chang, C.-L., "Tetrahedral-Mesh Simulations of Shock-Turbulence Interaction," AIAA Paper 2018-1529, 2018.
[31] Meneveau, C. and Katz, J., "Scale-Invariance and Turbulence Models for Large-Eddy Simulation," *Annu. Rev. Fluid Mech*. 32, pp. 1-32, 2000.
[32] Piomelli, U., Cabot, W. H., Moin, P., and Lee, S., "Subgrid-scale Backscatter in Turbulent and Transitional Flows," *Phys. Fluid A: Fluid Dynamics*, Vol. 3, 1766, 1991.
[33] Dunagan, S.E., Brown, J.L. and Miles, J.B. ," Interferometric Data for a Shock/Wave Boundary-Layer Interaction," NASA TM 88227, Sept. 1986
[34] Chang, S.-C., Chang, C.-L. and Venkatachari, B. S., "Cause and Cure – Deterioration in Accuracy of CFD Simulations with Use of High-Aspect-Ratio Triangular/Tetrahedral Grids," AIAA Paper, 2017-4293, 2017.
[35] Iyer, P. and Malik, M. R., "Large-Eddy Simulation of Axisymmetric Compression Corner Flow," AIAA Paper 2018-4031, 2018.